Accurate Surface Change Detection Method Using Phase of Coherence Function on SAR Imagery

Takehiro HOSHINO[†], Shouhei KIDERA[††a)], *and* Tetsuo KIRIMOTO[††], *Members*

SUMMARY   Satellite-borne SAR (synthetic aperture radar) is for high-resolution geosurface measurements. Recently, a feature extraction method based on CCD (coherent change detection) was developed, where a slight surface change on the geosurface is detected using the phase relationship between sequential complex SAR images of the same region made at different times. For accurate detection of the surface change, the log-likelihood method has been proposed. This method determines an appropriate threshold for change detection, making use of the phase characteristic of the changed area, and thus enhances the detection probability. However, this and other conventional methods do not seek to proactively employ phase information of the estimated coherence function, and their detection probability is often low, especially in the case that the target has small surface or local uniform changes. To overcome this problem, this paper proposes a novel transformation index that considers the phase difference of the coherence function. Furthermore, we introduce a pre-processing calibration method to compensate the bias error for the coherence phase which resulting mainly from the orbit error of the antenna platform. Finally, the results from numerical simulations and experiment modeling of the geosurface measurement verify the effectiveness of the proposed method, even in situations with low SNR (signal to noise ratio).

key words: *geosurface measurement, satelite-borne SAR, CCD, phase of coherence function*

1. Introduction

A high-resolution microwave imaging technique known as SAR is useful in geosurface measurements. Since the wavelength of a SAR system is in the centimeter range which is much longer than that of an optical sensor, SAR which has been developed in [1] has a significant advantage for application to surface imaging at times of cloudy weather or darkness. In past decades, various geosurface investigations based on the CCD method have been carried out, [2], [3], such as investigations on subsidence or uplift. CCD is simply based on correlation between sequential complex SAR local images obtained by temporally different observations of a same region. This technique has been shown to detect a slight change in the geosurface in the interval between the observations [4], [5]. In addition, Novak [6] reported that multi-polarization SAR offers more accurate change detection than single polarization SAR.

Recently, an accurate detection method based on a log-

likelihood criterion was proposed [7]. This method can determine the appropriate threshold for the change detection, and thus enhances the ROC (receiver operating characteristic) defined as the detection probability versus the false-alarm rate. However, it does not use phase information of the estimated coherence function, which deteriorates the detection probability, especially in the case that the target has small surface change or locally uniform change, which mainly contributes only a phase rotation to the coherence function.

To overcome this problem, this paper proposes a novel transformation index that is based on a consideration of the phase difference in the coherence function. In Sect. 2, the observation model is introduced and the coherence function and system model is defined. Section 3 presents the proposed detection index, which indicates the Euclidean distance of the obtained coherence on the Gaussian plane. In the proposed index calculation, the phase bias resulting mainly from baseline error is compensated for in data pre-processing. Section 4 presents the numerical simulation model. Finally, the experimental results described in Sect. 5 demonstrate that the proposed method attains higher ROC performance compared with the conventional method, even in noisy situations.

2. Observation Model and Coherent Change Detection

2.1 Observation Model

Figure 1 shows the observation geometry. It assumes there is a target with rough surface around the $z = 0$ plane, and that the propagation speed of the microwave is a known constant. A monostatic radar is assumed, and a set of scans
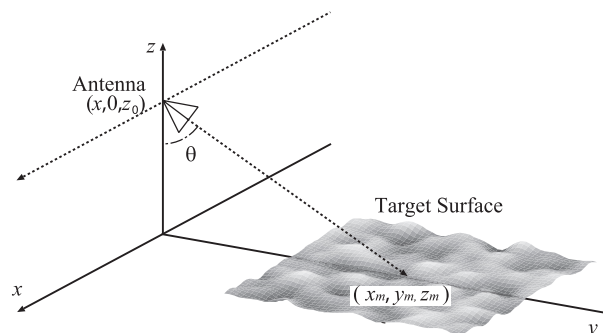

Fig. 1   Observation geometry.

are made along the line of $z = z_0$, $y = 0$ by a transmitting and receiving antenna, located at $(x, 0, z_0)$. The off-nadir angle is denoted by θ. We utilize a chirp-modulated pulse as the transmitting microwave and assume linear polarization in the direction of the y-z plane, which is referred to as vertical polarization, and thus, the receiving antenna obtains the polarized data at VV and VH polarization, where VV means V transmitting and V receiving polarizations and VH means V transmitting and H receiving polarizations.

2.2 Coherence Estimation of Complex SAR Images

This section describes the basics of the coherence estimation using the sequential complex SAR images, which are usually produced through back projection [8], [9]. $s_1(x, y)$ and $s_2(x, y)$ denote the complex SAR images of the target on the $z = 0$ plane before and after surface changes. The coherence function $\gamma(x, y)$ between the two SAR images is defined as [2]–[5]

$$\gamma(x_k, y_l) =$$
$$\frac{\displaystyle\sum_{m=-L/2}^{L/2} \sum_{n=-L/2}^{L/2} s_1(x_{k,m}, y_{l,n}) s_2^*(x_{k,m}, y_{l,m})}{\sqrt{\displaystyle\sum_{m=-L/2}^{L/2} \sum_{n=-L/2}^{L/2} |s_1(x_{k,m}, y_{l,n})|^2} \sqrt{\displaystyle\sum_{m=-L/2}^{L/2} \sum_{n=-L/2}^{L/2} |s_2(x_{k,m}, y_{l,n})|^2}}, \quad (1)$$

where * denotes a complex conjugate and $L\Delta l$ denotes the window size in the correlation. Δl is the sample interval along the x and y axes of the SAR image, and L determines the correlation length for the coherence estimation. $x_{k,m} = x_k + m\Delta l$ and $y_{l,n} = y_l + n\Delta l$. Obviously, $0 \le |\gamma(x_k, y_l)| \le 1$ holds. The conventional method evaluates only the amplitude of $\gamma(x, y)$, which is defined as [2]

$$\alpha(x, y) = |\gamma(x, y)|. \quad (2)$$

If $\alpha(x, y) \le \alpha_0$ holds, the region (x, y) is regarded as the "changed" region, where α_0 is set threshold. Otherwise, the region is estimated as "unchanged" region. Although this threshold provides robust change detection, it distorts the detection probability in the case that the change reflects only the phase of $\gamma(x, y)$. As such, when a target surface is uniformly raised, the norm of $\gamma(x, y)$ does not significantly change, but the phase can rotate considerably.

3. Proposed Detection Method

To enhance the detection probability, this paper introduces a novel detection index as follows. When $s_1(x, y) = s_2(x, y)$, obviously $\gamma(x, y) = 1$ holds. The proposed method then determines the threshold as the Euclidean distance from $\gamma(x, y)$ to $(1, 0)$ on the Gaussian plane. The novel index is defined as

$$\beta(x, y) = |1 - \gamma(x, y)|, \quad (3)$$

where $0 \le \beta \le 2$ holds. Substituting $\gamma(x, y) = A \exp(j\phi)$, Eq. (3) is rewritten as

$$\beta(x, y) = \sqrt{1 - 2A\cos\phi + A^2}, \quad (4)$$

where $0 \le A \le 1$ holds. Equation (4) indicates that this index allows change detection through consideration of the amplitude and phase difference between the complex SAR images. However, the phase of $\gamma(x, y)$ is mainly biased by the mismatch among sensor orbits, and should be appropriately compensated for in the calculation of $\beta(x, y)$.

As a data pre-processing for the proposed index calculation, the compensation scheme for the biased phase error is presented as follows. We assume that the error can be roughly estimated from the average coherence in the unchanged region. Since this biased error mainly reflects the coherence of the unchanged area with large norm of $\gamma(x, y)$, the compensation phase quantity is weighted as

$$\gamma_{\text{bias}} = \frac{\displaystyle\sum_{k=0}^{N_x-1} \sum_{l=0}^{N_y-1} |\gamma(x_k, y_l)|\gamma(x_k, y_l)}{\left| \displaystyle\sum_{k=0}^{N_x-1} \sum_{l=0}^{N_y-1} |\gamma(x_k, y_l)|\gamma(x_k, y_l) \right|}, \quad (5)$$

where N_x and N_y denote the total numbers of samples for the x and y axes. The compensated coherence $\gamma_0(x, y)$ is then obtained as

$$\gamma_0(x, y) = \gamma(x, y)\gamma_{\text{bias}}^*, \quad (6)$$

and is used in calculating $\beta(x, y)$.

Finally, the actual procedure of the proposed method is summarized as follows.

Step 1) Two SAR images $s_1(x, y)$ and $s_2(x, y)$ are obtained through back projection using observation data.

Step 2) Coherence $\gamma(x, y)$ is estimated for $s_1(x, y)$ and $s_2(x, y)$ using Eq. (1).

Step 3) The phase bias quantity as γ_{bias} is estimated using Eq. (5), and $\gamma_0(x, y)$ is obtained.
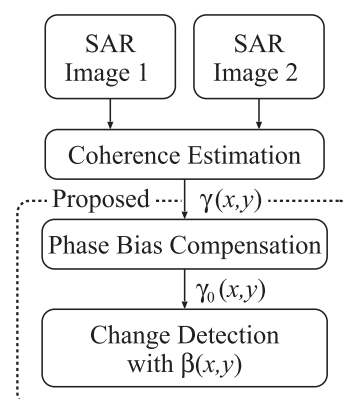

Fig. 2 Flowchart of the proposed detection method.

Step 4) The region (x, y) is regarded as the "changed" region, if the following condition is satisfied,

$$\beta(x, y) \geq \beta_0, \qquad (7)$$

where β_0 is the threshold for the change detection. Otherwise, the region is classified as the "unchanged" region.

Figure 2 illustrates a flowchart of the proposed method.

4. Performance Evaluation in Numerical Simulations

This section evaluates the performance of the proposed method through numerical simulation. Here, a rough-surface target is approximated as an aggregate of point targets. The signal received from these scattering points for each antenna location $(x, 0, z_0)$ is calculated as $S(x, f)$ [10]

$$S(x, f) = \begin{cases} \displaystyle\sum_{m=0}^{M-1} \frac{\exp\left(-\mathrm{j}\dfrac{4\pi f R(x, m)}{c}\right)}{R^2(x, m)}, & (f_{\min} \leq f \leq f_{\max}) \\ 0, & \text{(otherwise)} \end{cases}$$

$$(8)$$

where M denotes the total number of scattered points. $f_{\min}$ and $f_{\max}$ are the minimum and maximum frequencies, respectively. c is the speed of radio waves in air. $R(x, m) = \sqrt{(x - x_m)^2 + y_m^2 + (z_0 - z_m)^2}$, where (x_m, y_m, z_m) is a location of target point. Hamming window is applied for range-side-lobe suppression. The SAR image is then constructed using the back projection algorithm [8].

This validation simulates an approximately 1/100 scaled-down model of the actual spaceborne or airborne SAR system, where the target size, the height of the antenna scanning, or the spatial resolution is adjusted for this downsized scale. Figure 3 illustrates the observation model assumed in the numerical simulation. The synthetic aperture length is 1.6 m and z_0 = 1.48 m. $f_{\min}$ = 26 GHz and $f_{\max}$ = 40 GHz are set. The baseline errors are not considered in this evaluation. M = 160, 000 and the original target surface is modified by adding a height change with a uniform distribution from 0 to 1 cm and then smoothing with a
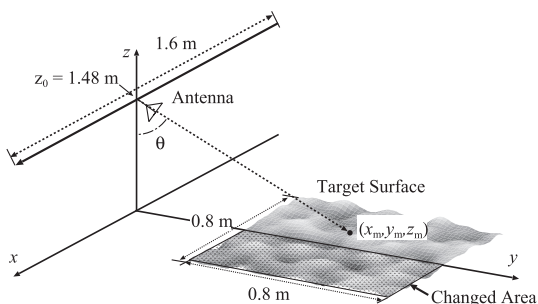
spatial averaging filter acting over an area of 2 cm × 2 cm. Then, tracks of a small tire are added to a half of the target surface, where each ditch of the tracks are 1 mm in depth and 8 mm in width. In addition, a part of the target surface (4% of the changed area) is uniformly uplifted with 0.1 mm, which mainly contributes only a phase difference of the two SAR images. The left and right-hand sides of Fig. 4 show the intensities of the complex SAR images before and after the target surface is changed, respectively. As confirmed in Fig. 4, there is hardly any difference between the two images. This is because the image intensity has little variation in the RCS (radar cross section) for such as small surface change. On the contrary, Fig. 5 shows the intensity of coherence $\gamma(x, y)$ calculated using Eq. (1) between the two SAR images shown in Fig. 4, where L = 11 and Δl = 0.25 cm. This figure illustrates the changed area of the target by locally cross-correlating the two complex SAR images.

Next, the ROC evaluation for each method is investigated. Here, P_D is the detection probability and P_N is the false-alarm rate, which are determined using the threshold for α_0 in the case of the conventional index $\alpha(x, y)$, and the threshold for β_0 in the case of the proposed index $\beta(x, y)$. Figure 6 depicts the ROC curve as P_D versus P_N for each method. Here, each data point for the region (x, y) is classified as part of the "changed" area, if it satisfies $\alpha(x, y) \leq \alpha_0$ in the conventional method or $\beta(x, y) \geq \beta_0$ in the proposed method. Otherwise, this point is regarded as part of the "unchanged" region. Any possible P_N is obtained by adjusting the threshold for α_0 or β_0. The figure verifies that the proposed index enhances P_D in the case that $P_N < 10^{-2}$.
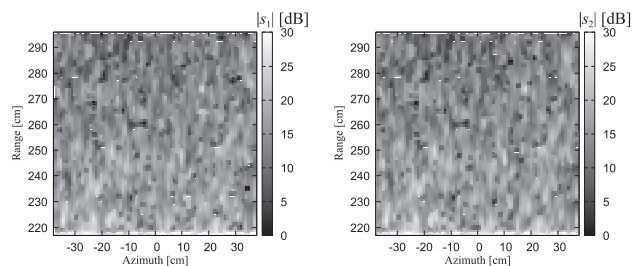

Fig. 4 Intensity of the complex SAR images obtained by simulation before (left) and after (right) the tire track was added.

Fig. 3 Arrangement for antenna and target with surface changed assumed in the numerical simulation.
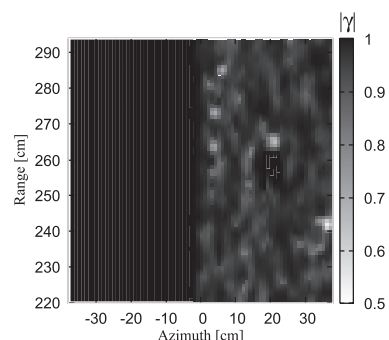

Fig. 5 Coherence intensity map of the complex SAR images in noiseless situation.
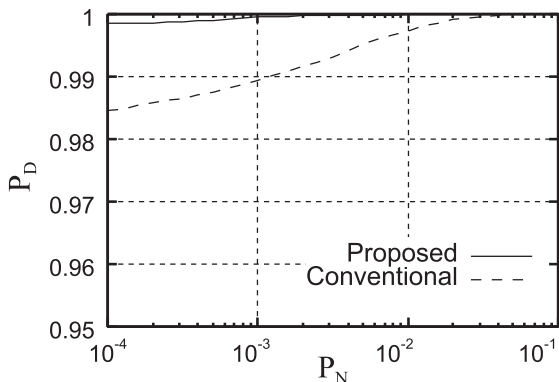
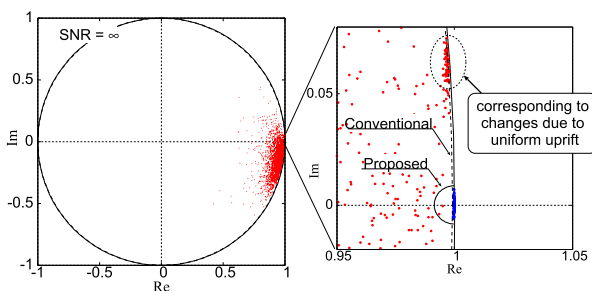**Fig. 6**   ROC evaluation for each method in noiseless situation.

Fig. 7   Distribution of $\gamma(x,y)$ obtained by numerical simulation in noiseless situation. (The red and blue points show the changed and unchanged target points. The broken and solid boundaries correspond to the conventional and proposed indices, where $P_N = 10^{-3}$ is required).

Fig. 8   ROC evaluation for each method in noisy cases for each SNR.

Fig. 9   Distributions of $\gamma(x,y)$ obtained by numerical simulation in noisy situations when SNR=35 dB(left) and 20 dB(right), and each definition is same as in Fig. 7.

Fig. 10   Example PDFs of $\alpha(x,y)$ (upper) and $\beta(x,y)$ (lower) at the case of SNR=35 dB, where their thresholds α_0 and β_0 are set to obtain $P_N = 10^{-3}$.

To verify the effectiveness of the proposed method, Fig. 7 presents the distribution of $\gamma(x,y)$ on the Gaussian plane. In this figure, each threshold as α_0 and β_0 is adjusted to obtain $P_N = 10^{-3}$, and the threshold circular boundaries satisfy $\alpha(x,y) = \alpha_0$ and $\beta(x,y) = \beta_0$, respectively. The unchanged area is shown as blue points and the changed area as red points. Here, the blue points retain higher values and are concentrated around the region of $\gamma(x,y) = 1$. As shown in the figure, the proposed method can recognize not only the changed $\gamma(x,y)$ concentrated around $(1, 0)$ but also changes outside the boundary determined by the conventional index (broken line in Fig. 7), which have large norms of $\gamma(x,y)$ but significant phase differences caused by the uniform uplift.

For investigation of a more noisy case, we numerically add Gaussian noise to the observation data. The SNR is the ratio of peak instantaneous signal power to the average noise power. Figure 8 shows the ROC for each method in noisy situations. For example, it is verified that the proposed method achieves P_D around 0.23, which is a 10% improvement over the performance of the conventional method at $P_N = 10^{-3}$ and SNR = 35 dB. The left and right-hand sides of Fig. 9 show distributions of $\gamma(x,y)$ on the Gaussian plane at SNR = 35 dB and SNR = 20 dB, respectively. The left-hand side of Fig. 9 shows that while the changed $\gamma(x,y)$ decreases its norm due to noise component, it has a different phase from the unchanged $\gamma(x,y)$, which contributes the discrepancy from the ROC obtained by the proposed method.
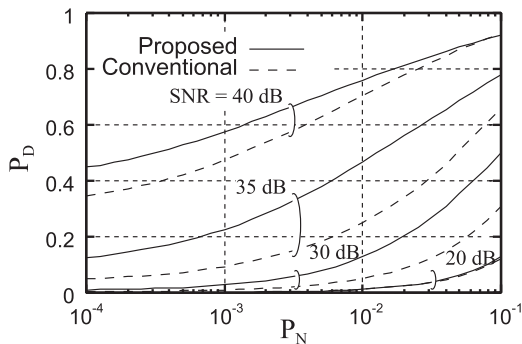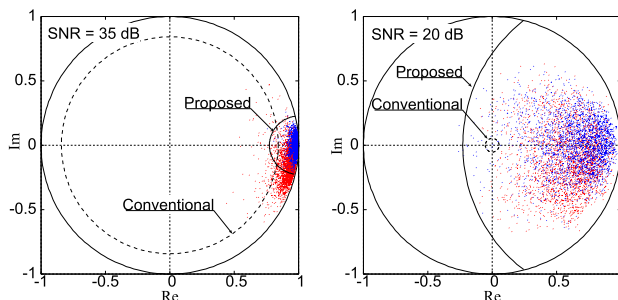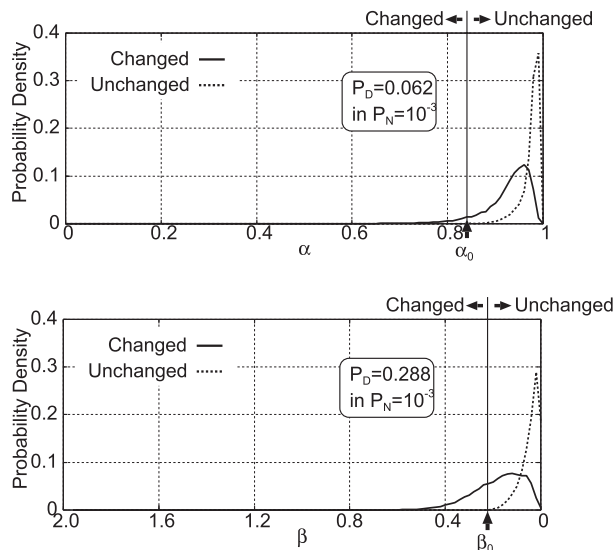
Furthermore, the upper and lower side of Fig. 10 depict an example of the probability density functions (PDFs) for the conventional index $\alpha(x,y)$ and the proposed index $\beta(x,y)$, in the case that SNR = 35 dB, respectively. The detection thresholds α_0 and β_0 are set to obtain $P_N = 10^{-3}$, and the figure demonstrates that the PDF of the proposed method is more suitable for detecting the areas of change, and has
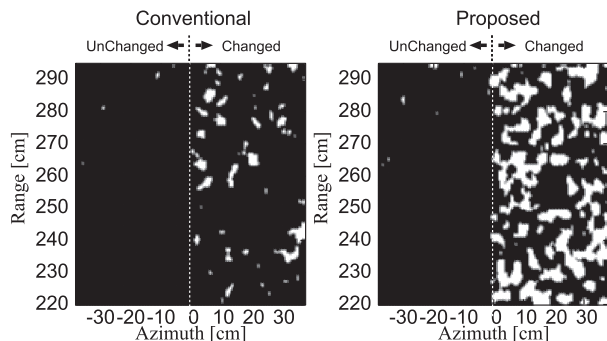
Fig. 11 Binary images discriminated by $\alpha(x, y)$ (left) and $\beta(x, y)$ (right) at SNR=35 dB, where the white region denotes the estimated "changed" area and the black region expresses the estimated "unchanged" area, where each threshold is determined for obtaining $P_N = 10^{-3}$.

higher detection probability owing to its discrimination of the phase difference of $\gamma(x, y)$. The left and right hand sides of Fig. 11 are the binary images discriminated by the conventional and proposed methods at SNR = 35 dB, respectively, where each threshold is set to obtain $P_N = 10^{-3}$. The figure visually verifies that the proposed method enhances the detection area for the changed region, compared with that of the conventional method with the lower false alarm rate.

On the contrary, in the lower SNR situation as shown in the right-hand side of Fig. 9, $|\gamma(x, y)|$ tends to converge around 0, in both unchanged and changed surfaces, because receiver noise is generally uncorrelated. Then, it is difficult to determine the appropriate threshold for an accurate change detection because both changed and unchanged points have almost the same distribution of $\gamma(x, y)$ even in Gaussian plane.

5. Performance Evaluation in an Experiment

This section presents a performance example in the experiment. Figure 12 shows the experiment geometry and Table 1 gives the parameters for the experimental setup. The 3 dB beam width of each horn antenna is 27 degrees, and the interval between the transmitting and receiving antennas is 4.8 cm. The height of scanning z_0 is 1.48 m. Figures 13 and 14 show SAR images obtained using the VV polarized radiation before and after the target surface changed, respectively. Each sample interval of SAR image Δl is 0.25 cm and the total x and y ranges of the target image are assumed as 70 and 65 cm, respectively. $L = 11$ is used in Eq. (1). The figures do not appear to confirm significant discrepancy between the two SAR images. Figures 15 and 16 are coherence intensity maps drawn from VV and VH polarized data, respectively. The SNR is 32 dB for the VV image and 17 dB for the VH image. In the case of VV as in Fig. 15, there is significant discrepancy between unchanged and changed areas. On the contrary, in the case of VH as in Fig. 16, the norm of $\gamma(x, y)$ for both unchanged and changed ares is high, and change detection is not trivial. The left and right-hand sides of Fig. 17 show the distributions of $\gamma(x, y)$ in the case
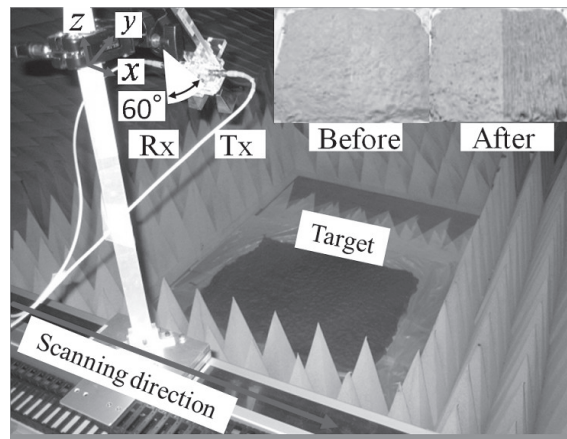

Fig. 12 Experimental setup.

Table 1 Experimental parameters.

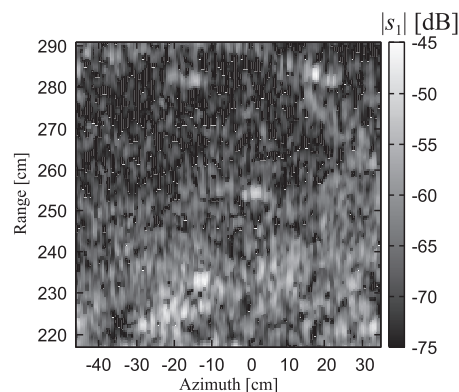|	
Center frequency	33 GHz
Frequency bandwidth	14 GHz
Slant range resolution	1.07 cm
Synthetic aperture length	1.6 m
Offnadir angle of antennas	60 deg
Target size (length, depth and thickness)	$80 \times 80 \times 3$ cm

Fig. 13 Intensity of the complex SAR images using VV polarized signals before the target surface was changed.

of changed and unchanged target points, respectively, before compensating the phase bias obtained using Eq. (6). Each threshold boundary as $\alpha(x, y) = \alpha_0$ and $\beta(x, y) = \beta_0$ is adjusted to obtain $P_N = 10^{-3}$. The figure demonstrates that the phase of $\gamma(x, y)$ for the unchanged area uniformly rotates, which it is mainly due to orbit error of the antenna platform. Figure 18 shows the ROC for each method in the case of VV and VH polarized radiation. Under the limit of the computational burden, the minimum value of P_N is set as 10^{-4}. The figure verifies that the proposed method enhances the detection probability by almost 10% in both VV and VH cases at the same $P_N = 10^{-3}$. This is because the proposed detection index $\beta(x, y)$ detects the phase difference of $\gamma(x, y)$, which
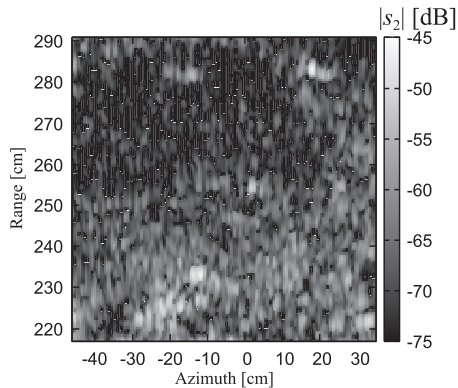
Fig. 14 Intensity of the complex SAR images using VV polarized signals after the target surface was changed.
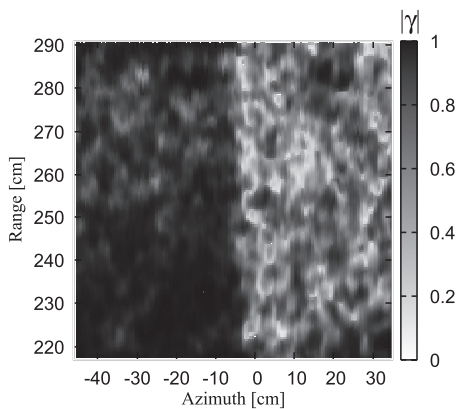

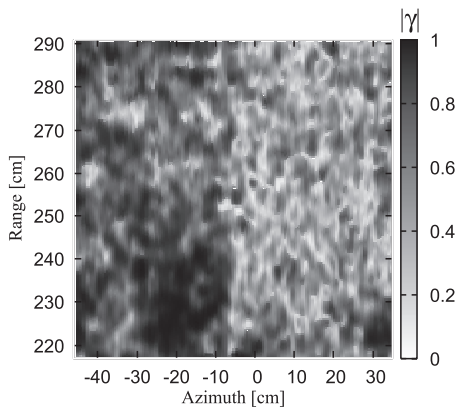**Fig. 15** Coherence intensity map of the complex SAR images using the VV polarized signals.

Fig. 16 Coherence intensity map of the complex SAR images using the VH polarized signals.

Fig. 17 Distribution of $\gamma(x, y)$ obtained by the experimental data using VV polarized signals before the phase biases compensation in Eq. (6).

Fig. 18 ROC evaluation for each method with the experimental data.

Fig. 19 Distribution of $\gamma(x, y)$ obtained by the experimental data using VV polarized signals after the phase biases compensation in Eq. (6).

is not considered when using the conventional index. Figures 19 and 20 illustrate the same view as Fig. 17 for the VV and VH cases, after compensating the phase bias in Eq. (6). The figures show that the proposed threshold is more suitable for change detection through accurately compensating the phase.

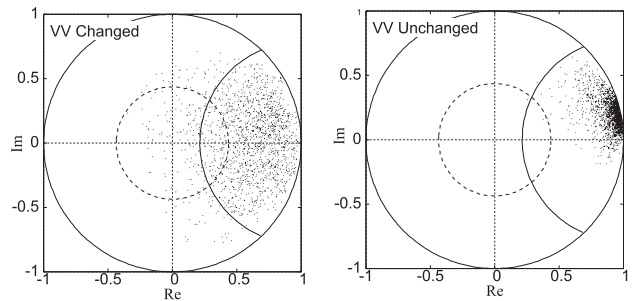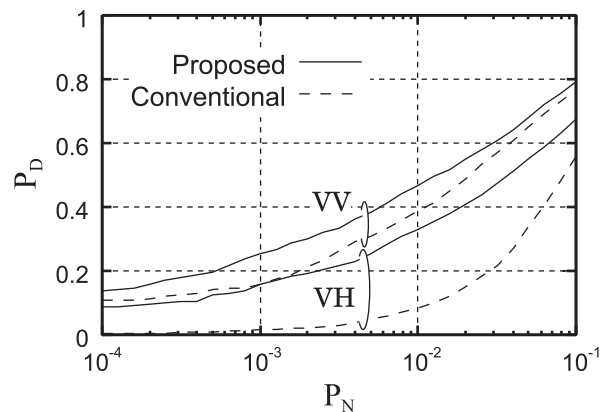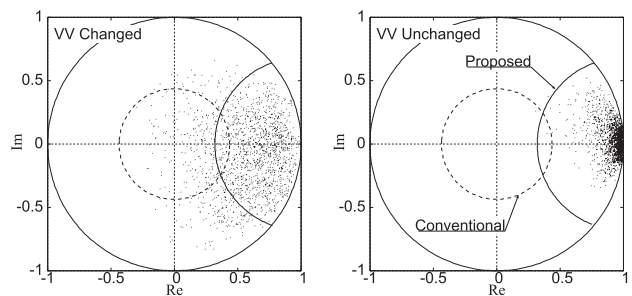As further validations, the upper and lower sides of

Fig. 21 show the PDFs for $\alpha(x, y)$ and $\beta(x, y)$, respectively, corresponding to the VV case as shown in Fig. 19. Each detection threshold is set to obtain $P_N = 10^{-3}$. In this case, the proposed method creates a more suitable PDF to discriminate the region of change, and its detection probability significantly increases. Moreover, the left and right hand sides of Fig. 22 respectively illustrate the binary images discriminated by the conventional and proposed indices in this case, where α_0 and β_0 are set for $P_N = 10^{-3}$. The figure also verifies that the proposed method enhances the detection area for the changed region with small P_N, compared with that of the conventional method. In addition, Figs. 23 and 24 show the same views as in Figs. 21 and 22, respectively, in the case of using the VH polarized data. As in the
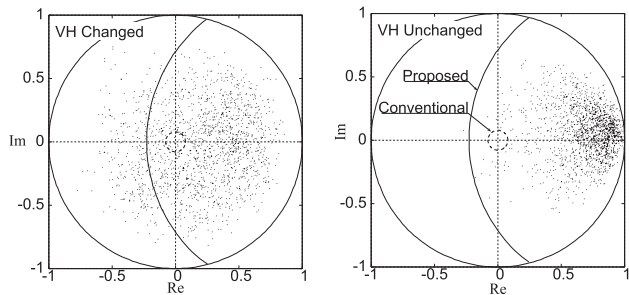
Fig. 20 Distribution of $\gamma(x, y)$ obtained by the experimental data using VH polarized signals after the phase biases compensation in Eq. (6).
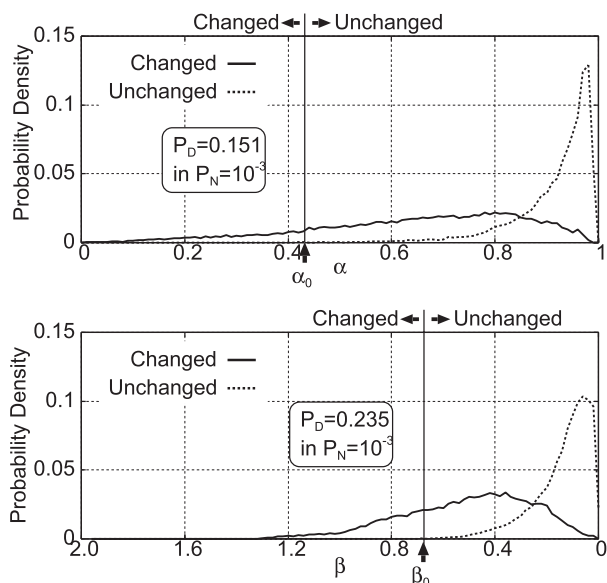

Fig. 21 Example PDFs of $\alpha(x, y)$ (upper) and $\beta(x, y)$ (lower) in using the VV polarized data, where their thresholds α_0 and β_0 are set to obtain $P_N = 10^{-3}$.
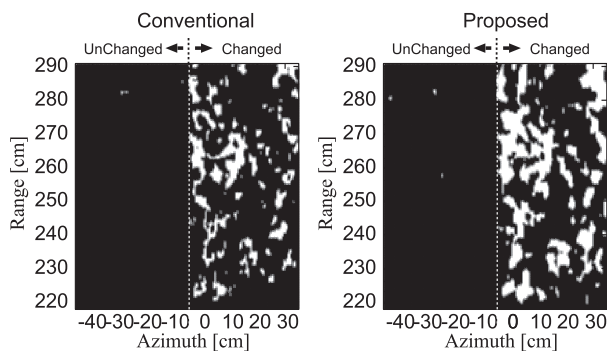

Fig. 22 Binary images discriminated by $\alpha(x, y)$ (left) and $\beta(x, y)$ (right) in using the VV polarized data, where the white region denotes the estimated "changed" area and the black region expresses the estimated "unchanged" area, where each threshold is determined for obtaining $P_N = 10^{-3}$.

result obtained using the conventional detection index, particularly on the left of Fig. 24, the area of change is hardly recognized, while the proposed method still provides detection probability of around 15%, even in such case of a lower
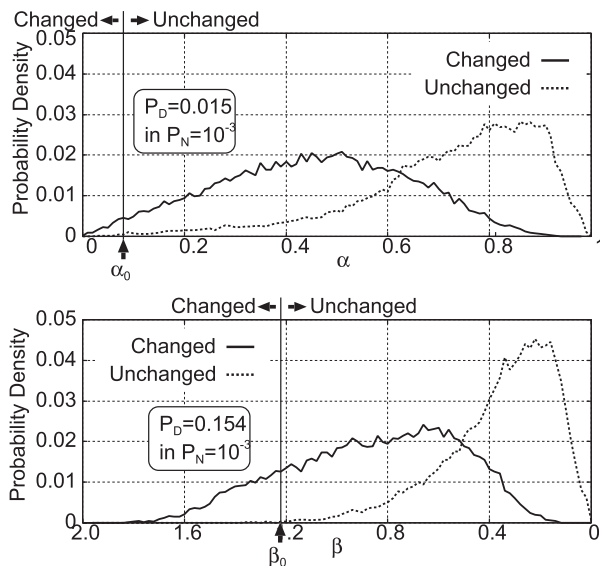

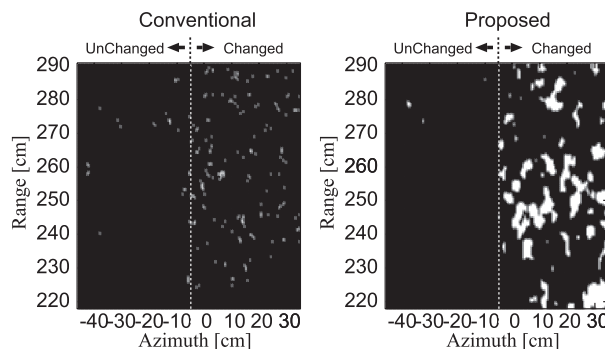**Fig. 23** Same view as in Fig. 21 in using VH polarized data.

Fig. 24 Same view as in Fig. 22 in using the VH polarized data.

SNR.

Note that, the phase fluctuations of γ in the changed region should be due to the components being intricately mixed by volume or double-bounced scattering effects, additive system noise, baseline errors [11]. Although the decomposition of these components seems useful for compensating the baseline errors or extracting the height change of target surfaces, this is a more challenging task that will be part of future work.

6. Conclusion

This paper proposed an accurate detection algorithm for geosurface change, considering the phase difference among sequential complex SAR images, which is not considered when using the conventional CCD index. The proposed method compensates the phase bias resulting from orbit error to increase the detection accuracy. In numerical simulation with a multiple-point scatterer model, the effectiveness of the proposed method was verified even in noisy situations using ROC evaluations. The notable advantage of our method is that it enhances the ROC performance between

SNR = 20 dB and 40 dB in comparison with the conventional index. Finally, the experimental study demonstrated that the proposed method achieved almost 10% higher detection probability compared with the conventional method in both VV and VH cases.

References

[1] W.M. Brown, "Synthetic aperture radar," IEEE Trans. Aerosp. Electron. Syst., vol.AES-3, pp.217–229, March 1967.

[2] R. Touzi, A. Lopes, J. Bruniquel, and P.W. Vachon, "Coherence estimation for SAR imagery," IEEE Trans. Geosci. Remote Sens., vol.37, no.1, pp.135–149, Jan. 1999.

[3] G. Franceschetti and R. Lanari, "Synthetic aperture RADAR processing," pp.185–195, CRC Press, New York, 1999.

[4] H.A. Zebker and J. Villasenor, "Decorrelation in interferometric radar echoes," IEEE Trans. Geosci. Remote Sens., vol.30, no.5, pp.950–959, Sept. 1992.

[5] E.W. Hoen and H.A. Zebker, "Penetration depths inferred from interferometric volume decorrelation observed over the Greenland ice sheet," IEEE Trans. Geosci. Remote Sens., vol.38, no.6, pp.2571–2583, Nov. 2000.

[6] L.M. Novak, "Coherent change detection for multi-polarization SAR," Signals, Syst. and Comput., 2005. Asilomar Conf., pp.568–573, 2005.

[7] M. Preiss, D.A. Gray, and N.J.S. Stacy, "Detecting scene change using synthetic aperture radar interferometry," IEEE Trans. Geosci. Remote Sens., vol.44, no.8, pp.2041–2054, Aug. 2006.

[8] L.M.H. Ulander, H. Hellsten, and G. Stenstrom, "Synthetic-aperture radar processing using fast factorized back-projection," IEEE Trans. Aerosp. Electron. Syst., vol.39, no.3, pp.760–776, July 2003.

[9] R. Goodman, S. Tummala, and W. Carrara, "Issues in ultra-wideband, widebeam SAR image formation," Proc. IEEE International Radar Conf., pp.479–485, Washington, D.C., May 1995.

[10] L. Tsang, J.A. Kong, K.H. Ding, and C.O. Ao, Scattering of Electromagnetic Waves: Numerical Simulations, pp.581–590, Wiley, New York, 2001.

[11] F. Gatelli, A.M. Guarnieri, F. Parizzi, P. Pasquali, C. Prati, and F. Rocca, "The wavenumber shift in SAR interferometry," IEEE Trans. Geosci. Remote Sens., vol.32, no.4, pp.855–865, July 1994.

Shouhei Kidera received his B.E. degree in Electrical and Electronic Engineering from Kyoto University in 2003 and M.I. and Ph.D. degrees in Informatics from Kyoto University in 2005 and 2007, respectively. He is an assistant professor in Graduate School of Informatics and Engineering, University of Electro-Communications, Japan. His current research interest is in advanced signal processing for the near field radar, UWB radar. He is an associate member of the Institute of Electrical and Electronics Engineering (IEEE) and the Institute of Electrical Engineering of Japan (IEEJ).

Tetsuo Kirimoto received the B.S. and M.S. and Ph.D. degrees in Communication Engineering from Osaka University in 1976, 1978 and 1995, respectively. During 1978–2003 he stayed in Mitsubishi Electric Corp. to study radar signal processing. From 1982 to 1983, he stayed as a visiting scientist at the Remote Sensing Laboratory of the University of Kansas. From 2003 to 2007, he joined the University of Kitakyushu as a Professor. Since 2007, he has been with the University of Electro-Communications, where he is a Professor at the Graduate School of Informatics and Engineering. His current study interests include digital signal processing and its application to various sensor systems. Prof. Kirimoto is a senior member of IEEE and a member of SICE (The Society of Instrument and Control Engineers) of Japan.

Takehiro Hoshino received his B.E. and M.E. degrees in Electronic Engineering from University of Electro-Communications in 2009 and 2011, respectively. He joined Mitsubishi Electric Corp. in 2011. His current research interest is in advanced signal processing for the SAR.